

End-to-End Physics Event Classification with the CMS Open Data: Applying Image-based Deep Learning on Detector Data to Directly Classify Collision Events at the LHC

M. Andrews¹, M. Paulini¹, S. Gleyzer², B. Poczós³

¹ *Department of Physics, Carnegie Mellon University, Pittsburgh, USA*

² *Department of Physics, University of Florida, Gainesville, USA and*

³ *Machine Learning Department, Carnegie Mellon University, Pittsburgh, USA*

(Dated: December 14, 2024)

We describe the construction of a class of general, end-to-end, image-based physics event classifiers that directly use simulated raw detector data to discriminate signal and background processes in collision events at the LHC. To better understand what such classifiers are able to learn and to address some of the challenges associated with their use, we attempt to distinguish the Standard Model Higgs Boson decaying to two photons from its leading backgrounds using high-fidelity simulated detector data from the 2012 CMS Open Data. We demonstrate the ability of end-to-end classifiers to learn from the angular distribution of the electromagnetic showers, their shape, and the energy scale of their constituent hits, even when the underlying particles are not fully resolved.

CONTENTS

I. Introduction	2
II. Open Data Simulated Samples	3
III. CMS Detector	3
A. Geometry	3
B. Reconstruction	4
IV. Detector Images	4
V. Network & Training	5
A. Network Architecture	6
B. Preprocessing & Mass de-correlation	7
C. Training	8
D. Evaluation	9
VI. Shower Classification	9
VII. Event Classification	10
A. Central η region	10
B. Central+Forward η region	12
VIII. Conclusions	13
Acknowledgments	15
References	15

I. INTRODUCTION

An important part of new physics searches at the Large Hadron Collider (LHC) involves classifying physics collision events to discriminate signal from background processes. At the Compact Muon Solenoid (CMS) [5], this is currently accomplished by first reconstructing the raw data collected by the detectors into progressively more physically-motivated quantities [7] until arriving at tabular-like particle-level data. The traditional analysis approach [2, 6] uses these condensed inputs to construct an event classifier that capitalizes on the decay structure or *topology* of the processes involved. While such approaches have been widely successful in understanding the Standard Model of Particle Physics (SM), they potentially lose information in the process—especially at the limits of detector resolution—that may hinder more exhaustive searches for physics Beyond the Standard Model (BSM).

In this paper, we propose a class of event classifiers that directly use raw detector data as inputs, or an *end-to-end* (E2E) event classifier. These are made possible by recent advances in Deep Learning and Convolutional Neural Networks (CNNs) in particular, that have allowed for breakthroughs in computer vision and pattern recognition with image-like data. At the same time, such E2E classifiers are also *general* event classifiers in that their construction is topology-independent, making them well-suited to merged and variable decay structures. In theory, one could train on the entire SM and beyond with the same network, regardless of topological complexities.

While the full potential of E2E classifiers lies in probing challenging BSM models, we choose a simple but illustrative process to better understand what such classifiers are able to learn, and to address some of the challenges involved in their application to searches for new physics. While others have used CNNs in the context of jet classification [11, 16] and event classification on whole detector images [12, 13], or Recursive Neural Networks for jet clustering [18], this is the first application of an end-to-end classifier for event classification using high-quality LHC detector data. We thus explore the decay of the Standard Model Higgs boson to diphotons using the 2012 CMS Simulated Open Data, which uses the highest grade of detector simulation, building on earlier work presented in [1].

This paper is organized as follows: in Section II we introduce our data sample and event selection. Then, in Section III we briefly describe the CMS geometry and detector image construction in Section IV. In Section V, we outline our network & training procedure. We then review results related to particle identification in Section VI and present event classification results in Section VII. Finally, our conclusions are summarized in Section VIII.

II. OPEN DATA SIMULATED SAMPLES

The CMS Open Data provides a number of high-quality, simulated 2012 CMS data that permit us to evaluate the E2E approach. They use the highest grade of detector simulation available, using **Geant4** [4] to model the interaction of particles with the detector material and the most detailed geometry model of CMS. This is the same state-of-the-art detector simulation as used for CMS detector performance studies.

Datasets. For our signal sample, we choose the gluon fusion Higgs to diphoton dataset [10], $gg \rightarrow H \rightarrow \gamma\gamma$, with a Higgs mass of $m_H = 125$ GeV. For the background samples, we choose the two leading processes by cross-section: quark fusion to prompt diphoton [8], $q\bar{q} \rightarrow \gamma\gamma$, or the so-called Born diphoton production, and $\gamma + \text{jet}$ production [9]. The $\gamma\gamma$ background is an *irreducible* background in that it also contains two photons in the final state, differing only in kinematics with the $H \rightarrow \gamma\gamma$ photons. In the $\gamma + \text{jet}$ background, the jet is electromagnetically enriched so as to deposit primarily in the Electromagnetic Calorimeter via a neutral meson decaying to two *merged* photons. The jet thus appears as a single photon-like cluster. While there are other backgrounds involved in the Higgs to diphoton decay, the above two are representative of the most challenging types: kinematically-differentiated decays ($\gamma\gamma$) and particle shower-differentiated decays due to unresolved objects ($\gamma + \text{jet}$). All the above samples account for the multi-parton interactions from the underlying event as well as pile-up (PU). The PU distributions are run era dependent, ranging from a peak average PU of $\langle \text{PU} \rangle = 18 - 21$ [3].

Event selection We categorize the samples based on pseudorapidity η , where $\eta = -\ln[\tan(\theta/2)]$ and θ is the spherical polar angle with respect to the beam axis. The **central** sample is restricted to $|\eta| < 1.44$ and the **central+forward** sample to $|\eta| < 2.3$, with the region around the Electromagnetic Calorimeter Barrel-Endcap boundary, $1.44 < |\eta| < 1.54$, excluded. For both categories, we require exactly two reconstructed photons, each with transverse momentum $p_T > 20$ GeV. Since the number of events is limited and not balanced between datasets, with the lowest statistics coming from the $\gamma\gamma$ dataset, we apply no further isolation cuts. We require, however, that the reconstructed mass of the diphoton system be $m_{\gamma\gamma} > 90$ GeV. With these cuts, we obtain 63502 and 135602 events in the $\gamma\gamma$ dataset for the central and central+forward categories, respectively. These are broken down by run era in Table I.

Category	Run2012AB	Run2012C	Run2012D
Central	16308	24538	22206
Central+forward	35141	47885	52576

TABLE I: Number of selected events by run era, per $|\eta|$ category, per dataset.

For the remaining datasets, we take the first N_i events fulfilling the same era i breakdown, to minimize learning based on differences in pile-up.

III. CMS DETECTOR

The Compact Muon Solenoid (CMS) detector is arranged as a series of concentric cylindrical sections—including a barrel section and circular endcap sections—that encase a central interaction point where the LHC proton beams collide. Each cylindrical detector section or *subdetector* is specialized at measuring one or more aspect of the particles decaying from the collision. Together, the information from the different subdetectors is used to paint as complete a picture as possible about the collision event, or *event* for short.

A. Geometry

The subdetectors of interest to us are those in the Inner Tracking system (Tracker), the Electromagnetic Calorimeter (ECAL), and the Hadronic Calorimeter (HCAL). The Tracker is the innermost cylindrical part of CMS and is responsible for detecting the hits associated with the tracks left by charged particles as they fly outward from the interaction point. This is reflected in the use of fine silicon segments which provide precise spatial resolution but no practical energy measurement. In 2012, it was composed of 13 barrel layers and 14 layers per endcap. To avoid particles slipping through cracks in the layers, the barrel and endcap layers overlap in pseudorapidity in a non-trivial way. Each layer is composed of fine strip- or pixel-like silicon segments, depending on layer, which provide the spatial localization. Moreover, the barrel and endcap sections of the Tracker are segmented differently: in cylindrical coor-

dinates, with the beamline as axis, they are in axis and azimuth (z, ϕ) in the barrel and in radius and azimuth (ρ, ϕ) in the endcap, with the dimensions of the segments changing with layer.

Surrounding the Tracker system is the ECAL subdetector. The ECAL measures the energy deposits of electrons and photons by capturing almost all their energy using scintillating lead tungstate crystals. In the barrel section (EB), which spans $|\eta| < 1.479$, it is segmented by pseudorapidity ($i\eta_{\text{EB}}$) and azimuth ($i\phi_{\text{EB}}$) giving a 170×360 crystal arrangement, respectively. This gives the EB an average granularity of $\Delta\eta_{\text{EB}} \times \Delta\phi_{\text{EB}} = 0.0174 \times 0.0174$. In the endcap sections (EE+/EE-), which span $1.479 < |\eta| < 3.0$, the crystals are arranged in a Cartesian grid (iX, iY) with 7324 crystals per endcap. For reference, most electrons/photons will deposit $> 90\%$ of their energy within a 3×3 window. The ECAL thus provides a potent combination of spatial and energy resolution.

Surrounding the ECAL is the HCAL subdetector. The HCAL measures the energy deposits of hadronic particles—primarily charged pions and kaons making up hadronic jets—using scintillating brass towers. In both barrel (HB) and endcap (HE+/HE-) sections, the HCAL is segmented in pseudorapidity ($i\eta_{\text{HCAL}}$), azimuth ($i\phi_{\text{HCAL}}$), and readout depth (d_{HCAL}). The depth segmentation varies in a non-trivial way with $|\eta|$ but is uniform in ϕ . Combined, the HB and HE span the range $|\eta| < 3$, with the boundary between the two occurring at $|\eta| = 1.566$. The HCAL is considerably more coarse than the ECAL at $\Delta\eta_{\text{HCAL}} \times \Delta\phi_{\text{HCAL}} = 0.087 \times 0.087$, or about 5×5 EB crystals per HB tower. Starting at $|i\eta_{\text{HCAL}}| > 20$, however, the ϕ granularity in HE becomes more coarse still with $\Delta\phi_{\text{HCAL}} = 0.174$. Note that $i\phi_{\text{HCAL}} = 1$ does *not* correspond to the same plane as $i\phi_{\text{ECAL}} = 1$.

To avoid particles slipping through cracks undetected, none of the barrel-endcap boundaries between the Tracker, ECAL, and HCAL overlap.

B. Reconstruction

Below, we briefly describe how the particle interactions with the detector are used to reconstruct the detector hits which form the basis of the low-level data used in the E2E approach. For reference, we also provide an overview of how this low-level detector data are used to form the higher-level particle data conventionally used for physics analyses.

Calorimeter Hit Reconstruction. Both the ECAL and HCAL share similar strategies to energy reconstruction of calorimeter hits [5]. As an electromagnetic (hadronic) particle enters the ECAL (HCAL), an electromagnetic (hadronic) shower is produced. This is detected as a signal pulse which is digitized into a series of amplitudes versus time—essentially a short video of the shower growth and decay in each ECAL crystal (HCAL tower). By applying a fit to these digitized amplitudes, one derives the energy and timing associated with that hit. These are then calibrated to give a final reconstructed energy and time (among other quantities) per crystal (tower), known collectively as the *reconstructed hit*.

Tracker Hit & Track Reconstruction. In contrast, as charged particles pass through the finely segmented Tracker, they deposit very little energy in the silicon. As such the Tracker hits provide precise position information for use in charged particle track reconstruction but no practical energy information. Using the hits recorded in the different layers of the Tracker, a combinatorial Kalman-filter pattern recognition algorithm [5] is used to iteratively fit charged particle tracks through the Tracker hits starting from the seed layer. From these *reconstructed track* fits, one can then obtain various track parameters. Notably, these include the track’s position at the point of closest approach to the beamline, and its transverse momentum from its bending in the magnetic field of the CMS solenoid.

High-level Particle Reconstruction. The reconstructed tracks and calorimeter hits are the basic inputs to the rule-based CMS Particle Flow algorithm [7] which constructs intermediate-level data before producing the final, high-level particle data. These include attributes like probable particle identity, kinematics, and shower shape features. These serve as the primary inputs to most CMS analyses and event classifiers. In contrast, for the E2E approach, the inputs are the reconstructed tracks and calorimeter hits. Due to the unavailability of Tracker hits in CMS Open Data, we use the reconstructed *tracks* rather than the raw *hits*. A similar approach was taken in [13].

IV. DETECTOR IMAGES

The CMS Open Data makes available the reconstructed hits for the ECAL and HCAL. This makes it possible to construct calorimeter images whose pixels correspond exactly to physical crystals (towers). This is important because not all crystals (towers) have the exact same dimensions and so images created using averaged dimensions will incur some distortion. This level of accuracy would not be possible when using intermediate-level data like *CaloTowers* (which are only binned at the coarser HCAL) or the particle-level data (which are disconnected from the calorimeter

geometry altogether).

Combining Images. The main challenge in combining subdetector images arises not from differences in granularity but from differences in *segmentation* and the fact that regions of dissimilar segmentation overlap. For subdetector sections which do not spatially overlap (e.g. the ECAL barrel with the ECAL endcap) these images can be kept separate. However, for subdetector sections which do overlap, such as the ECAL barrel and the HCAL barrel calorimeters, the depth information is compromised if the images are not combined at the input level. Even though, in 2-dimensional CNNs, convolutions are not performed along the depth axis, the activations along the depth axis are still summed over.

Therefore, to investigate the trade-off between detector fidelity and image integration, we experiment with different geometry strategies: we choose a subdetector S to represent with the highest fidelity and project all other subdetectors S' to the segmentation and boundaries of S , introducing a deformation and potentially some information loss on the S' images. Procedures for constructing ECAL- and HCAL-centric geometries are described below and visualized for a single $\gamma + \text{jet}$ event in Figure 1.

ECAL Images. The ECAL image is defined in terms of reconstructed hit energies versus ECAL crystal coordinates. These are distinct for the EB and the EEs since they have different segmentation (see Section III A). For the EB, we construct an unrolled rectangular 170×360 image. For the EEs, we inscribe each circular EE section in a square 100×100 image. These define the ECAL-centric geometry. Alternatively, for the HCAL-centric geometry, we can construct a contiguous ECAL image by projecting the (iX, iY) -segmented EEs onto an EB-like $(i\eta, i\phi)$ segmentation. These are then stitched to the ends of the EB image to form a single 280×360 image that spans the same η range as the HCAL. Since this results in sparse showers in the endcap regions, we smear out each hit over a 2×2 window. While these are potentially lossy transformation on the EEs, it will allow us to combine the full ECAL range with the HCAL into a single composite image.

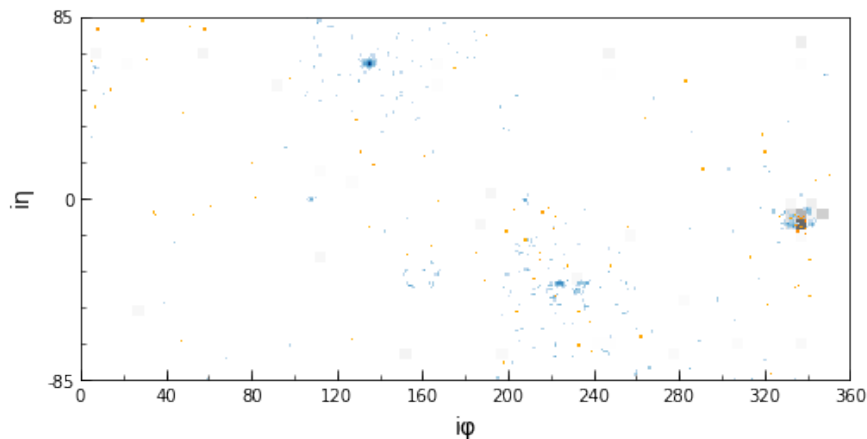
HCAL Images. The HCAL image is defined in terms of reconstructed hit energies versus HCAL tower coordinates. These are shared by the HB and the HEs due to their similar segmentation. Since most events ($\approx 99\%$) in our samples only deposit in the first HCAL depth, we approximate the HCAL as a single depth by summing over d_{depth} for a given $(i\eta_{\text{HCAL}}, i\phi_{\text{HCAL}})$. In addition, some towers overlap in physical η and are summed over as well to provide consistent alignment with the ECAL image. Above $|i\eta_{\text{HCAL}}| > 20$, where the ϕ granularity is halved (see Section III A), we share the energy across two $i\phi_{\text{HCAL}}$ towers. We can thus construct a single, contiguous 56×72 image for the combined HB and HE. Without loss of information, this image is upsampled by a factor of 5 to produce a 280×360 HCAL image. This defines the HCAL-centric geometry. For the ECAL-centric geometry, the portions of this image which overlap with EB are left untouched while those which overlap with the EEs are detached and projected from their native $(i\eta, i\phi)$ segmentation onto an EE-like (iX, iY) segmentation, giving a 100×100 image per endcap.

Tracker Images. Because of the lack of Tracker hits in the CMS Open Data, the tracker image is constructed as a 2D histogram of the reconstructed tracks' positions versus either an ECAL- or HCAL-centric geometry. To help discriminate against the numerous pile-up tracks, each track entry is weighted by its transverse momentum. Only *high-purity* tracks, or tracks with the highest level of fit quality, are used.

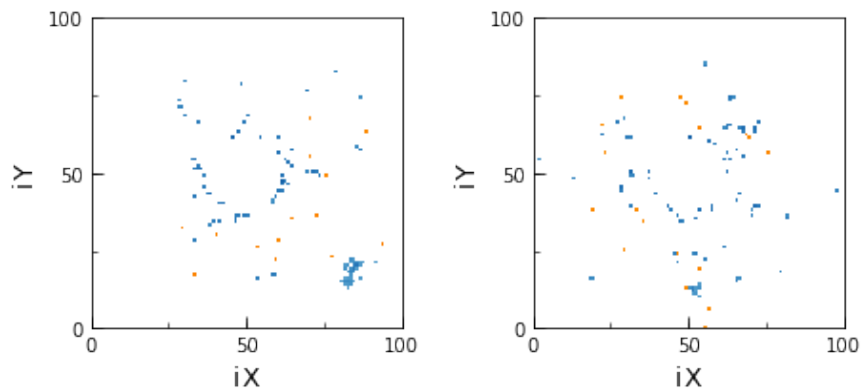
For the central category, we use only the subdetector images which overlap with the EB (Figure 1a) giving image inputs of resolution 170×360 . For the central+forward category, we use images which overlap with both the EB+EE (ECAL-centric: Figures 1a+1b or HCAL centric: Figures 1a+1c). These give image inputs of resolution 170×360 and 100×100 for the ECAL-centric geometry, and 270×360 for the HCAL-centric one. Lastly, while the event selection (Section II) applies η cuts on the selection of candidate photons, no such cuts are applied in the construction of the actual detector images in this paper, although this remains an option for future work.

V. NETWORK & TRAINING

At the heart of the end-to-end classifier is a Convolutional Neural Network (CNN). In this Section, we describe how these deep learning networks are applied in order to extract information from the various subdetector images (see Section IV) in a way that best complements each subdetector's knowledge of the event. Afterwards, we discuss some of the challenges associated with using end-to-end classifiers, how we train them, and how we evaluate their performance in this study.



(a) Barrel section of composite image in ECAL-centric geometry. Image resolution: 170×360 .



(b) Endcap sections of composite image in ECAL-centric geometry. Image resolution: 100×100 .

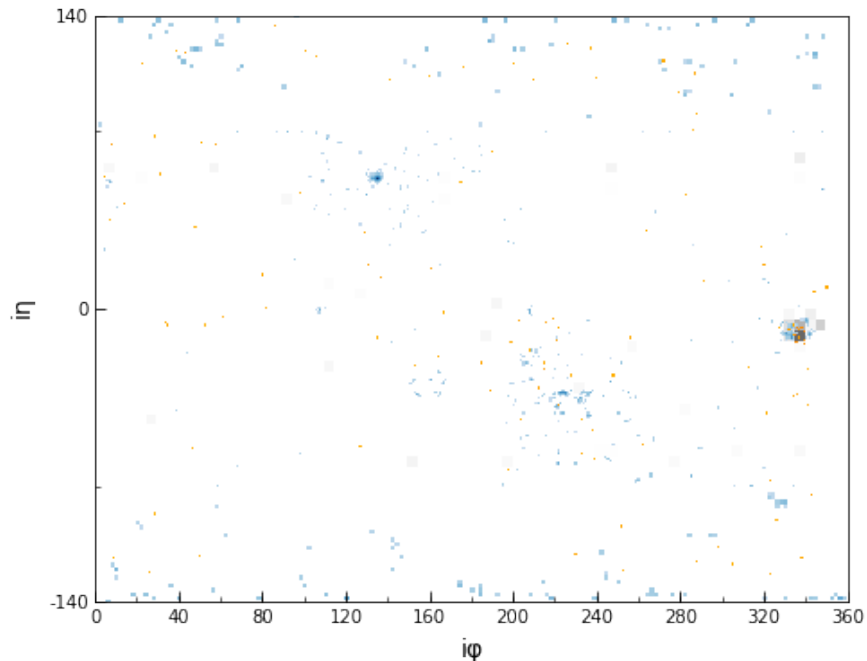
A. Network Architecture

For all image-based or **end-to-end (E2E) event classifiers**, Residual Net-type networks (ResNet-15) are used due to their simplicity and scalability with image size and network depth [15]. A representative network is illustrated in Figure 2a. Due to the sparse nature of the data, the best performance is obtained when using MaxPooling operations in place of AveragePooling and with no batch normalization. For samples in the central category, we use a single ResNet-15. For those in the central+forward category with ECAL-centric geometry we use a separate ResNet-15 for each of barrel, endcap-, and endcap+. They are concatenated at the output of their final GlobalMaxPooling layer before being fed to a Fully-Connected Network (FCN), as illustrated in Figure 2c. In the central+forward HCAL-centric geometry, we use a single ResNet-15. The various E2E classifier models are summarized in Table II.

Model	Category	Architecture	Inputs
EB	Central	ResNet-15	ECAL*
CMS-B	Central	ResNet-15	Tracker, ECAL, HCAL*
ECAL	Central+Fwd	3 x ResNet-15, FCN	ECAL
CMS-I	Central+Fwd	3 x ResNet-15, FCN	Tracker, ECAL, HCAL
CMS-II	Central+Fwd	ResNet-15	Tracker, ECAL, HCAL

TABLE II: Summary of end-to-end models used in this paper. *NOTE: Models from the central category only use the Barrel portion of the subdetector images (c.f. Figure 1a).

Within the available statistics, the E2E results do not benefit from deeper networks or the inclusion of a FCN in the case of single ResNet-15. Other variations on concatenating the networks for multiple images were attempted but were found to be less performant.



(c) Composite image in HCAL-centric geometry. Extent of EB indicated by minor ticks on y-axis. Image resolution: 280×360 .

FIG. 1: Composite images of a single $\gamma + \text{jet}$ event in different geometry strategies: separate Barrel (1a) and Endcaps (1b) for the ECAL-centric geometry, and stitched together (1c) for the HCAL-centric. Tracks are in yellow log scale, ECAL hits in blue log scale, and HCAL hits in gray linear scale. Additional zero suppression applied for clarity. Note the photon at around $(i\eta = 70, \phi = 130)$ which is free of HCAL hits or Tracks. In contrast, the jet at around $(i\eta = -10, \phi = 340)$ shows contributions from all three subdetectors. Only the Barrel images (1a) are used for classification in the central category (see Section II).

To serve as a reference for conventional event classifiers, we train a separate 3-layer, 256-node FCN on the reconstructed 4-momenta of the two candidate photons in each event, which we denote as the **4-momentum classifier**. Specifically, these are trained on the transverse momenta of the photons divided by the diphoton mass, $p_{T,i}/m_{\gamma\gamma}$, their pseudorapidities η_i , and the cosine of their azimuthal separation, $\cos(\phi_1 - \phi_2)$, where $i = 1, 2$ is the photon index. The division by $m_{\gamma\gamma}$ ensures the classifier is not correlated with the mass of the Higgs boson [6]. Note that this classifier serves as a purely kinematical reference and does not take into account information about the shape of the photon showers. The 4-momentum classifier results were not sensitive to the depth and width of the FCN network.

B. Preprocessing & Mass de-correlation

Preprocessing plays a major role not just in improving the network optimization process but in controlling the physics content of the inputs themselves. In particular, for an event classifier intended for a resonance search, it is desirable for the classifier's output to *not* be correlated with the mass of the signal resonance. Since one typically applies a cut on the classifier score to obtain a signal-enriched sample, this mitigates the risk of sculpting a false peak in the background.

Mass-sculpting—as it is commonly called—is especially an issue for irreducible backgrounds that differ only by kinematics. To measure it, we use the Cramér-von Mises (CVM) metric suggested in [20] and implemented in approximate form in [21]. We calculate this on the classifier's signal score vs. reconstructed diphoton mass for true $\gamma\gamma$ events, as illustrated in Figure 4a.

To achieve mass de-correlation, we divide each image by the reconstructed diphoton mass for that event. To first approximation, this has the effect of mapping the diphoton system to unit invariant mass for both signal and background. Using the scalar sum of the diphoton $p_{T\text{'s}}$ (i.e. neglecting the angular component) is also effective. In fact, any quantity that maps the diphoton invariant mass for both signal and background events to a similar distribution

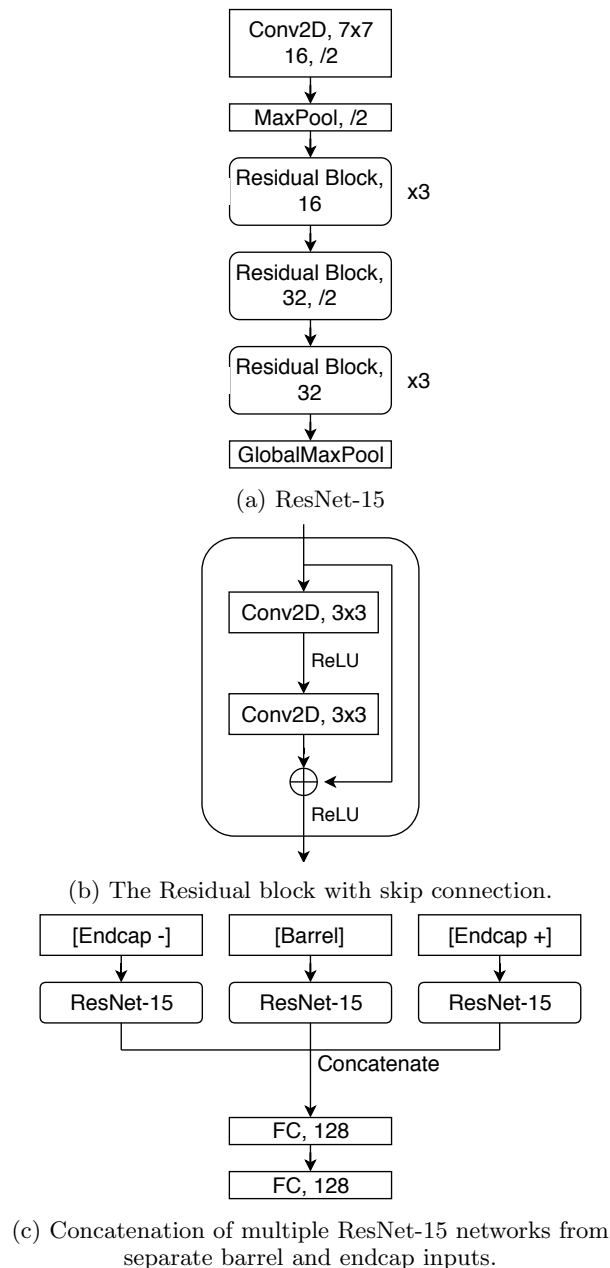


FIG. 2: The Residual Net (ResNet) architecture, as used for single (2a) and multiple (2c) image inputs.

achieves a similar effect. There are, however, additional subtleties, the details of which will be treated in a separate paper.

C. Training

We train for three-class ($H \rightarrow \gamma\gamma$ vs. $\gamma\gamma$ vs. $\gamma + \text{jet}$) classification with the normalized classification scores for each class label given by the softmax function. We use the ADAM adaptive learning rate optimizer [17] to minimize the cross-entropy loss. In general, we use an initial learning rate of 5×10^{-4} , batch size of 32, and implement early stopping if no progress is seen beyond 5 epochs. In addition, we implement an early stopping criteria based on the CVM metric, of $\text{CVM} < 0.002$ for the central category and $\text{CVM} < 0.004$ for the central+forward category. The breakdown of training and test set—which doubles as the validation set—is shown in Table III. Both training and validation sets contain balanced samples of the three classes. All training was done using the PyTorch [19] software

library running on a single NVIDIA Titan X GPU.

Category	Training Events per class	Test Events per class
Central	51200	11800
Central+forward	120000	15600

TABLE III: Number of events in training and test sets *for each class*. Test set doubles as validation set due to limited statistics. The total training and test sets contain a balanced number of class samples.

Note that, in this paper, priority is given to presenting a broad and consistent survey of E2E classifiers over individual classifier optimization. As such, individual classifier hyper-parameter tuning was kept to a minimum, although we found the above training parameters to be fairly robust across the different E2E classifiers.

D. Evaluation

We use the area under the curve (AUC) of the normalized Receiver Operating Characteristic (ROC) as the main figure of merit in this paper. As is common in High Energy Physics, the ROC curve is interpreted in terms of the signal sample efficiency (true positive rate) vs. background sample rejection (true negative rate). To evaluate the multi-class classification results, we define a per-class (1-vs-Rest) ROC and select the classifier with the best ROC AUC score in the signal label, subject to constraints on the CVM metric. To better understand the performance between the individual backgrounds in the multi-class classifier, for each background, we also present the (1-vs-1) signal vs. single background component of the ROC in the signal label. While the latter helps to give a sense of the individual background performance, it should be noted that multi-class classification is an inherently coupled problem, as is the nature of physics event classification. Lastly, as noted in Table III, the evaluation is done on a *balanced* mix of class samples. While this is not necessarily the case in reality, it allows for an unbiased assessment of classifier performance in this simplified context.

VI. SHOWER CLASSIFICATION

For reference, we recap our earlier results [1] in end-to-end classification of electromagnetic showers, or particle identification in the ECAL. Using the same image construction techniques described in Section IV, we successfully discriminated electron- (e^-) vs. photon- (γ) induced showers with ECAL Barrel images. While not such a practical concern when track information is taken into account, when the ECAL information is taken in isolation, to first approximation, electron- and photon-induced showers appear identical. Indeed, it is only through higher-order effects like bremsstrahlung (due to the electron’s interaction with the CMS solenoid) that the electron shower becomes slightly smeared and asymmetric in ϕ —an effect that is practically impossible to discern by eye.

In Table IV, we present the best-in-category results of using Convolutional Neural Network-based (**CNN**), Convolutional Long Short-Term Memory-based (**Conv-LSTM**) Recurrent Neural Networks [14], and Fully-Connected Neural Networks (**FCN**) on 32×32 ECAL images centered on the shower maximum constructed out of various raw data inputs. These indicate a preference for convolutional-based architectures and suggest it is sufficient to use reconstructed hit energies (see Section III B) to attain best results. Moreover, the range of these scores serves to illustrate just how sensitive end-to-end classifiers are at processing raw detector information even when the showers appear indistinguishable to the naked eye.

Category	Network, Input	ROC AUC
CNN	VGG, energy	0.807
LSTM	Conv-LSTM, digis	0.799
FCN	3-layers, digis	0.770

TABLE IV: Best-in-Category results of e^- vs. γ shower classification on 32×32 ECAL Barrel images. *Energy* inputs correspond to reconstructed hit energies, while *digis* correspond to the series of digitized amplitudes vs. time (see Section III B).

As a further step, we take the whole EB image instead of just the shower crop. The e^- vs. γ results are shown in Table V. We see there is minimal loss in performance, owing to the CNN’s ability to learn features in a translationally-invariant way. More importantly, we see a marked improvement in the classification of particle pairs (e^+e^- vs. $\gamma\gamma$)

due to the CNN’s having learned that the shower pairs must be either *both* electron-like or both photon-like, instead of attempting to classify them independently. This suggests that topological complexity works in favor the end-to-end approach and that the greatest gains may yet come from more challenging topologies.

Classification	Network, Input	ROC AUC
e^- vs. γ	ResNet, energy	0.788
e^+e^- vs. $\gamma\gamma$	ResNet, energy	0.997

TABLE V: Results of shower classification on full ECAL Barrel images.

In sum, these results illustrate the ability of end-to-end classifiers to discern fine shower details in granular detectors like the CMS Electromagnetic calorimeter. However, when dealing with particles from real physics decays, there is the additional complexity introduced by *kinematics*, which we turn our attention to next.

VII. EVENT CLASSIFICATION

In any real physics decay, energy and momentum conservation impose physical constraints on the allowed kinematics of the decaying particles. The case of Higgs boson decays and its related backgrounds is no exception. For the $\gamma\gamma$ background, the shower types are, in fact, identical and any differences are entirely kinematical. For the $\gamma + \text{jet}$ background, in addition to kinematical differences, one of the particles is of a different type, so the opportunity exists for exploiting differences in the shower shape, as we have already seen in the previous Section VI. Moreover, in a realistic physics scenario, the classifier must also simultaneously discriminate between multiple decay processes. In this section, we therefore attempt to classify $H \rightarrow \gamma\gamma$ vs. $\gamma\gamma$ vs. $\gamma + \text{jet}$ decays.

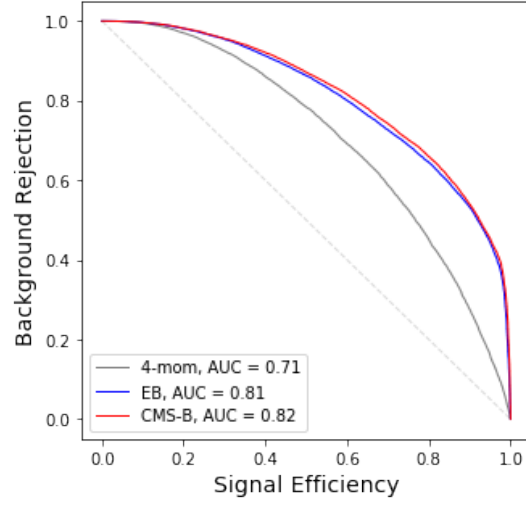
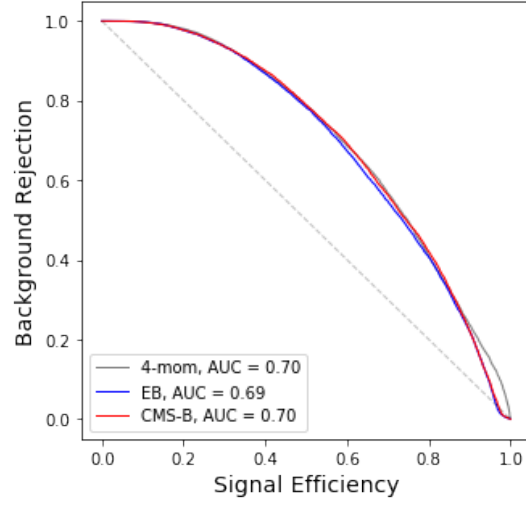
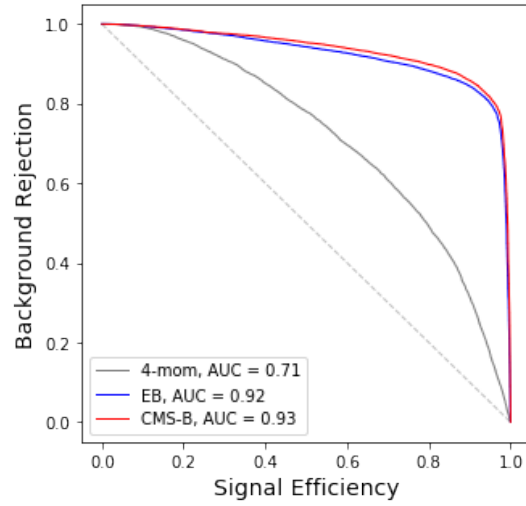
The end-to-end (E2E) event classification results are divided by pseudorapidity (see Section II), with the results for the central (central+forward) category given in Table VI (Table VII), and corresponding ROC curves in Figure 3 (Figure 5). The ECAL-only classifier is labeled **EB (ECAL)** and the Tracks+ECAL+HCAL classifier in the ECAL-centric geometry is labeled **CMS-B (CMS-I)**. For the central+forward region, we also include the results of the HCAL-centric classifier (**CMS-II**). In each category, we plot the signal vs. combined background ROC (1-vs-Rest), as well as the signal vs. single background ROC component (1-vs-1) (see Section V D). For context, we also include the results of the (mass de-correlated) 4-momentum-only classifier (**4-mom**) and the mass-aware ECAL-only classifier (**EB/ECAL, mass-aware**). Note that the results represent evaluations on balanced class samples (see Section V D).

A. Central η region

	Metric	4-mom	EB, mass-aware	EB	CMS-B
ROC AUC, 1-vs-Rest					
$H \rightarrow \gamma\gamma$	0.708	0.926	0.807	0.815	
$\gamma\gamma$	0.807	0.923	0.837	0.844	
$\gamma + \text{jet}$	0.803	0.954	0.948	0.960	
ROC AUC, 1-vs-1					
$H \rightarrow \gamma\gamma$ vs $\gamma\gamma$	0.702	0.894	0.690	0.697	
$H \rightarrow \gamma\gamma$ vs $\gamma + \text{jet}$	0.714	0.959	0.923	0.933	
CVM	0.002	0.080	0.002	0.002	

TABLE VI: Multi-class Event Classification Results, central $|\eta| < 1.44$ region.

To understand these results, we first focus on the central category where we only use detector images from the Barrel section of CMS. From the 1-vs-Rest plot (Figure 3a), we see that, overall, image-based classifiers perform better than purely kinematical classifiers. This is, of course, expected in the presence of an irreducible background but serves to confirm that the E2E classifier is delivering as expected. We also see that the **EB** and **CMS-B** classifiers perform comparably, with only negligible advantage to including additional subdetectors. Since the $\gamma\gamma$ is an exclusively ECAL signature, and the $\gamma + \text{jet}$ a majority ECAL signature, this is again in line with expectation. However, looking back at the sample event image in Figure 1, we see that other subdetectors carry quite a bit of noise from pile-up and underlying event so it is not *a priori* obvious that the **CMS-B** classifier should perform as well as the **EB** under these circumstances. Therefore, that no sizable degradation in performance was seen by including additional noisy subdetectors highlights the E2E classifier’s ability to effectively screen out irrelevant features from extraneous images.

(a) $H \rightarrow \gamma\gamma$ vs. Rest(b) $H \rightarrow \gamma\gamma$ vs. $\gamma\gamma$ component.(c) $H \rightarrow \gamma\gamma$ vs. γ + jet component.FIG. 3: Multi-class Event Classification ROC curves, central $|\eta| < 1.44$ region.

Lastly, we note that the highest performance—by a substantial margin—is achieved when the E2E classifier is allowed to learn the Higgs boson mass, or is *mass-aware* (see Table VI). Since the classifier tends to learn the mass, this tells us that mass de-correlation is, in general, a destructive operation. To gain further insight, we next turn to the individual background components.

Looking at the $H \rightarrow \gamma\gamma$ vs. $\gamma\gamma$ component (Figure 3b), we see that for kinematically-differentiated backgrounds, the E2E classifiers perform comparably to the 4-momentum-only classifier. This is important because it demonstrates that, at least in this context, we have paid no penalty in using a *general* classifier trained on raw data over a *specialized* kinematical classifier that relied on our ability to reconstruct the event. Therefore, in the limit that the particle kinematics can be fully reconstructed, we observe the E2E approach to perform similarly. Next, while mass de-correlation is clearly a lossy operation (see Table VI), it does not completely kill classifier performance even for irreducible backgrounds. This suggests the kinematical information is manifested in the detector image in two ways: the angular distribution of the photon showers and the *energy scale* of the shower hits. While mass de-correlation removes the latter, it preserves the former, allowing for residual performance.

Turning now to the $H \rightarrow \gamma\gamma$ vs. $\gamma + \text{jet}$ component (Figure 3c), we see that this is primarily responsible for the E2E advantage over kinematics-only. This is expected because the jet (typically, merged $\pi^0 \rightarrow \gamma\gamma$) is not fully resolved and is instead reconstructed as a single photon in the 4-momentum case, which we have not supplemented with additional shower shape information. Despite appearing as a single photon-like cluster, the jet manifests itself in the ECAL image as a *differentiated* shower, which, on occasion, is discernible by eye (see Figure 1). As reviewed in Section VI, E2E classifiers are highly sensitive to differences in shower shapes even when no distinguishing kinematical information is present. Moreover, the $\gamma + \text{jet}$ decay exhibits similar non-resonant kinematics to $\gamma\gamma$ and so, to the 4-momentum classifier, the two should look alike. This is confirmed by their similar 4-momentum results (c.f. Figure 3b). Lastly, owing to strong shower differentiation, the effect of mass de-correlation on the $\gamma + \text{jet}$ background is much subdued. We can thus conclude that the impact of mass de-correlation depends strongly on the importance of kinematics—in particular, of the energy scale—over shower differentiation. For predominantly kinematically-differentiated decays, the effect of de-correlation will be substantial while for primarily shower-differentiated decays, the effect will be minimal. In Figure 4, we plot the classifier score in the signal label vs. diphoton mass for the two backgrounds to illustrate the impact of mass de-correlation.

B. Central+Forward η region

	Metric	4-mom	ECAL, mass-aware	ECAL	CMS-I	CMS-II
ROC AUC, 1-vs-Rest						
	$H \rightarrow \gamma\gamma$	0.727	0.933	0.805	0.803	0.806
	$\gamma\gamma$	0.812	0.921	0.828	0.829	0.826
	$\gamma + \text{jet}$	0.810	0.955	0.941	0.943	0.951
ROC AUC, 1-vs-1						
	$H \rightarrow \gamma\gamma$ vs $\gamma\gamma$	0.711	0.705	0.702	0.692	0.688
	$H \rightarrow \gamma\gamma$ vs $\gamma + \text{jet}$	0.743	0.740	0.908	0.914	0.923
	CVM	0.003	0.088	0.002	0.003	0.003

TABLE VII: Multi-class Event Classification Results, central+forward $|\eta| < 2.3$ region.

In this category, we have included the Endcap images either in ECAL-centric (**ECAL, CMS-I**) or HCAL-centric (**CMS-II**) fashion (see Sections IV and V A). In general, we find the main conclusions from the Central category to still be relevant for the Central+Forward category with minimal differences in absolute performance. This alone is important because it informs us about the scalability of E2E network architectures and their ability to deal with the increased pile-up of the forward detector regions. Despite drastic differences in network structures, we find classifier performance to not be greatly sensitive to the choice of Endcap projection. This is arguably a testament to the flexibility and robustness of Convolutional Neural Networks. Where present, any differences are small enough that a more detailed study of the associated uncertainties would be needed to make conclusive statements. Moreover, in the interest of presenting a broad and consistent survey of E2E techniques, we reiterate that we have employed a uniform set of hyper-parameters across all E2E classifiers (see Section V). For future work focusing on specific E2E implementations, we expect performance optimization to take greater priority.

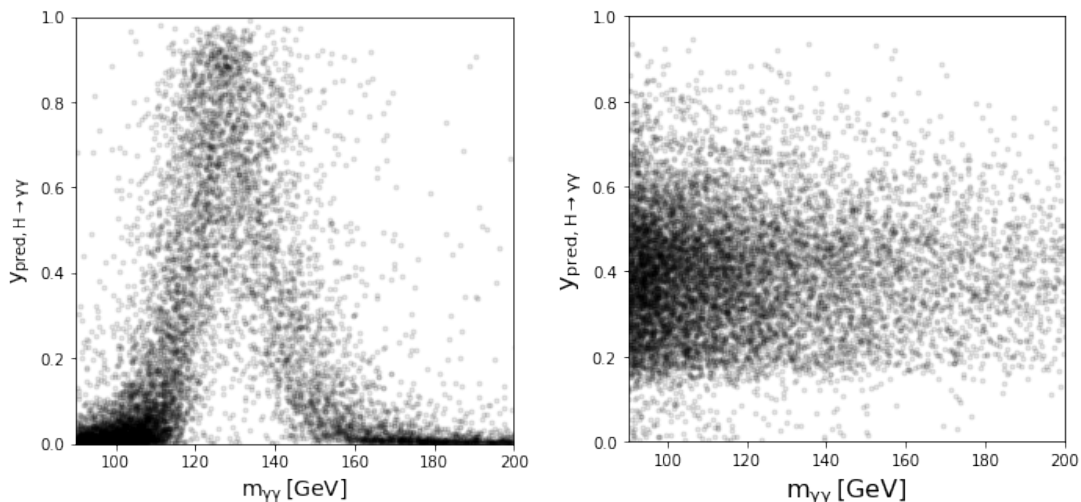
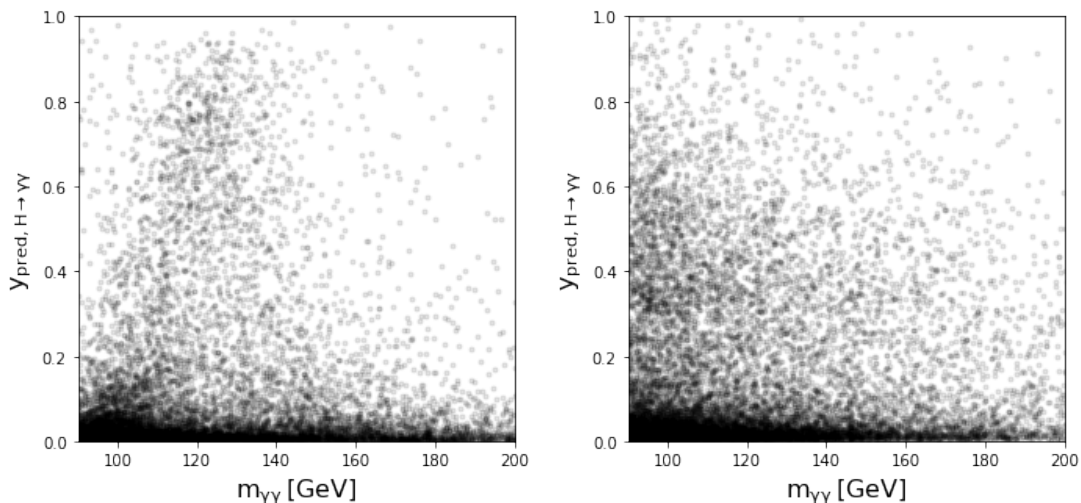
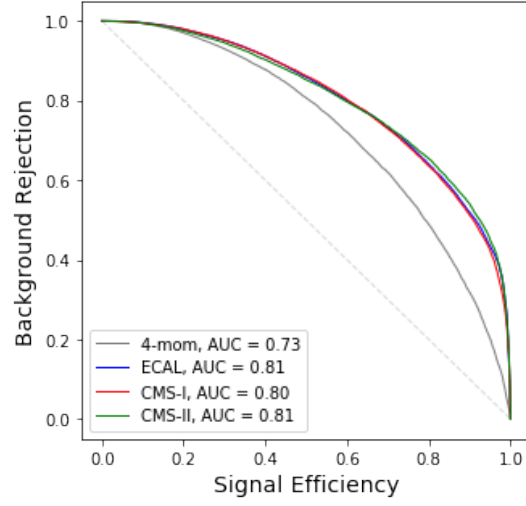
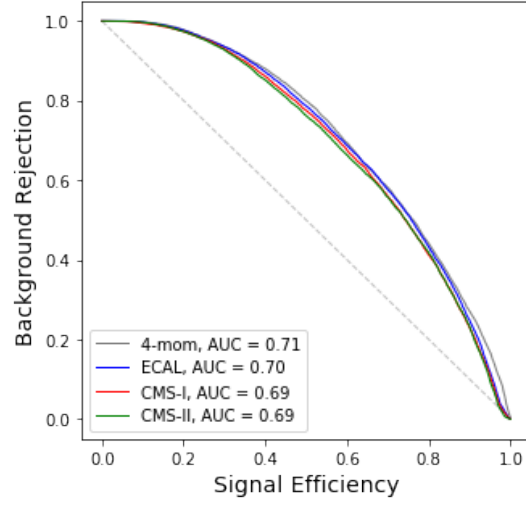
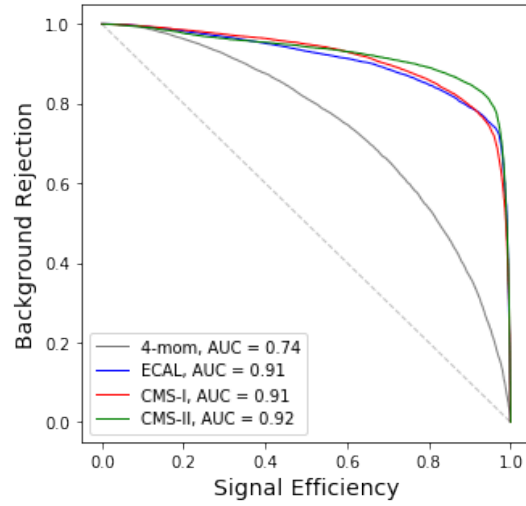
(a) True $\gamma\gamma$ events, without mass de-correlation (left) and with (right).(b) True $\gamma + \text{jet}$ events, without mass de-correlation (left) and with (right).

FIG. 4: Central **EB** classifier score in signal label vs. reconstructed diphoton mass for true $\gamma\gamma$ (4a) and $\gamma + \text{jet}$ (4b) events, with and without mass de-correlation. The impact of de-correlation is more severe if the background lacks shower differentiation.

VIII. CONCLUSIONS

In this paper, we described the construction of a class of *general*, end-to-end, image-based event classifiers, using high-fidelity, simulated, raw detector data as inputs. Their use is not restricted to any particular topology and they are not reliant on one's ability to reconstruct the event kinematics and can therefore be applied to arbitrarily complex topologies without modification. To combine overlapping subdetector images of dissimilar segmentation, we chose one subdetector to render faithfully and projected all other subdetectors to its segmentation, allowing for different geometry strategies. While these classifiers are best suited to challenging decays, we have applied them in a simplified search for the Standard Model $H \rightarrow \gamma\gamma$ decay to highlight their key features and challenges. Through the irreducible $\gamma\gamma$ background, we were able to infer that such classifiers are able to learn about the angular distribution of the photon showers as well as the energy scale of their constituent hits. By removing the latter through preprocessing, we showed that we were able to de-correlate the event classifier from the reconstructed diphoton mass while still preserving the former. Through the reducible $\gamma + \text{jet}$ background, we additionally showed that such classifiers can learn about the photon shower shape giving them a strong advantage over purely kinematical classifiers while being less reliant on the energy scale information. Finally, we demonstrated the scalability and flexibility of these classifiers when dealing with

(a) $H \rightarrow \gamma\gamma$ vs. Rest(b) $H \rightarrow \gamma\gamma$ vs. $\gamma\gamma$ component.(c) $H \rightarrow \gamma\gamma$ vs. γ + jet component.FIG. 5: Multi-class Event Classification ROC curves, central+forward $|\eta| < 2.3$ region.

multiple detector images and networks where we found them to be robust versus the choice of geometry projection and the inclusion of extraneous, noisy detector images.

ACKNOWLEDGMENTS

We would like to thank the CMS Collaboration and the CERN Open Data group for releasing their simulated data under an open access policy. We strongly support initiatives to provide such high-quality simulated datasets that can encourage the development of novel but also realistic algorithms, especially in the area of machine learning. We believe their continued availability will be of great benefit to the high energy physics community in the long run.

-
- [1] M. Andrews, M. Paulini, S. Gleyzer, and B. Poczos. Exploring end-to-end deep learning solutions for event classification at CMS, 2017. <https://indico.cern.ch/event/567550/contributions/2629451>.
 - [2] P. Baldi, P. Sadowski, and D. Whiteson. Searching for exotic particles in high-energy physics with deep learning. *Nature Communications*, 5(4308), 2014.
 - [3] CERN. PdMVPileUpDescription2012, PU_RD1, May 2017.
 - [4] GEANT4 Collaboration. GEANT4: A Simulation toolkit. *Nucl. Instrum. Meth.*, A506, 2003.
 - [5] The CMS Collaboration. The CMS experiment at the CERN LHC. *JINST*, 3, 2008.
 - [6] The CMS Collaboration. Observation of the diphoton decay of the Higgs boson and measurement of its properties. *Eur. Phys. J. C*, 74(3076), 2014.
 - [7] The CMS Collaboration. Particle-flow reconstruction and global event description with the CMS detector. *JINST*, 12, 2017.
 - [8] The CMS Collaboration. Simulated dataset DiPhotonBorn_Pt-25To250.8TeV_ext-pythia6 in AODSIM format for 2012 collision data, 2017. CERN Open Data Portal.
 - [9] The CMS Collaboration. Simulated dataset GJet_Pt40_doubleEMEnriched_TuneZ2star_8TeV_ext-pythia6 in AODSIM format for 2012 collision data, 2017. CERN Open Data Portal.
 - [10] The CMS Collaboration. Simulated dataset GluGluHToGG_M-125.8TeV-pythia6 in AODSIM format for 2012 collision data, 2017. CERN Open Data Portal.
 - [11] L. de Oliveira, M. Kagan, L. Mackey, B. Nachman, and A. Schwartzman. Jet-Images—Deep Learning Edition. *JHEP*, 07(069), 2016.
 - [12] A. Aurisano et al. A Convolutional Neural Network Neutrino Event Classifier. *JINST*, 11, 2016.
 - [13] W. Bhimji et al. Deep Neural Networks for Physics Analysis on low-level whole-detector data at the LHC, 2017. <https://indico.cern.ch/event/567550/contributions/2629673>.
 - [14] X. Shi et al. Convolutional LSTM Network: A Machine Learning Approach for Precipitation Nowcasting. 2015.
 - [15] K. He, X. Zhang, S. Ren, and J. Sun. Deep residual learning for image recognition. In *2016 IEEE Conference on Computer Vision and Pattern Recognition, CVPR 2016, Las Vegas, NV, USA, June 27-30, 2016* [15], pages 770–778.
 - [16] G. Kasieczka, T. Plehn, M. Russell, and T. Schell. Deep-learning Top Taggers or The End of QCD? *JHEP*, 05(006), 2017.
 - [17] D. P. Kingma and J. Ba. Adam: A Method for Stochastic Optimization. 2014.
 - [18] G. Louppe, K. Cho, C. Becot, and K. Cranmer. QCD-Aware Recursive Neural Networks for Jet Physics. 2017.
 - [19] A. Paszke, S. Gross, S. Chintala, G. Chanan, E. Yang, Z. DeVito, Z. Lin, A. Desmaison, L. Antiga, and A. Lerer. Automatic differentiation in pytorch. In *NIPS-W*, 2017.
 - [20] A. Rogozhnikova, A. Bukvac, V. Gligorovd, A. Ustyuzhaninb, and M. Williams. New approaches for boosting to uniformity. *JINST*, 10, 2015.
 - [21] Yandex Data School. Flavours of Physics Challenge Evaluation, May 2017. <https://github.com/yandexdataschool/flavours-of-physics-start/blob/master/evaluation.py>.